PAPER

Tunable acoustic waveguides in periodic arrays made of rigid square-rod scatterers: theory and experimental realization

To cite this article: V Romero-García *et al* 2013 *J. Phys. D: Appl. Phys.* **46** 305108

IOP PUBLISHING JOURNAL OF PHYSICS D: APPLIED PHYSICS

J. Phys. D: Appl. Phys. **46** (2013) 305108 (11pp) doi:10.1088/0022-3727/46/30/305108

Tunable acoustic waveguides in periodic arrays made of rigid square-rod scatterers: theory and experimental realization

V Romero-García[1,2], C Lagarrigue[2], J-P Groby[2], O Richoux[2] and V Tournat[2]

[1] Instituto de investigación para la gestión integrada de zonas costeras, Universitat Politècnica de València, Paranimf 1, 46730 Gandia, Spain

[2] LUNAM Université, CNRS, Université du Maine, LAUM, Av. O. Messiaen, 72085, Le Mans, France

E-mail: virogar1@gmail.com

Received 24 April 2013, in final form 9 June 2013
Published 5 July 2013
Online at stacks.iop.org/JPhysD/46/305108

Abstract

The tunable and the engineering possibilities of waveguides in periodic arrays made of rigid square-rod scatterers are theoretically and experimentally reported in this work. Due to the square shape of the scatterers, the control of their orientation with respect to the direction of the incident wave can be used for moulding the propagating acoustic waves inside the periodic structure. On the one hand, the plane wave expansion with supercell approximation is used to obtain the band structure of the periodic system. On the other hand, the scattering of waves in finite periodic arrays is analysed using the finite elements method. Experimentally, a prototype made of rigid square-rod scatterers is used to validate the theoretical predictions. A spatial-frequency filter and some applications in waveguiding for audible sound are discussed in this work. Good agreement between theory and experiments and the high tunability of the system are demonstrated.

(Some figures may appear in colour only in the online journal)

1. Introduction

Wave propagation through periodic structures is a subject of interest for several branches of science and technology such as water waves [1], seismology [2], acoustics [3–5] or electromagnetism [6, 7]. The most important property of such systems is perhaps the presence of band gaps, ranges of frequencies in which wave propagation is forbidden [8–11]. Many interesting physical phenomena arise from this property such as wave localization [12, 13], excitation of evanescent waves [14, 15], as well as relevant applications concerning filtering [16] and wave guiding [17]. Therefore the control of the properties of the band gaps, specially the creation of large full band gaps, has been deeply analysed [18] during recent years.

Band gaps in periodic structures appear at high symmetry points in the Brillouin zone due to the presence of a degeneracy of the band structure [10]. The most severe limit to increase the width of the band gap comes precisely from this degeneracy and, as a consequence, many approaches have been proposed to lift the band degeneracy and thus enlarge the band gaps [19–21]. In this sense, one possibility consists of reducing the total symmetry of the crystal in order to remove some band degeneracy, allowing the appearance of complete gaps [8]. Another possibility to enlarge band gaps comes from changing the shape of the scatterers. In this way, some theoretical works have shown that for a given lattice symmetry, the width of the gap is the largest when the geometric symmetry of each scatterer is the same as that of the lattice which, incidentally, has the same symmetry as the first Brillouin zone [22]. For example, square-rod scatterers arranged following a two-dimensional (2D) square unit cell have theoretically exhibited a progressive widening of the gap by increasing the rotation angle of these rods with respect

to the lattice orientation [23]. Other theoretical works have used optimization techniques to improve the band structure by changing the shape of the scatterers, using for example fractal patterns [24]. Very recently, Bilal and Hussein [25] have reported several optimized unit-cell designs exhibiting record values of normalized band gap size for combined in-plane and out-of-plane elastic waves. Specifically, they report a design with a normalized band gap width exceeding 60% for the case of combined polarizations. Finally, band gaps can be also tuned by anisotropic scatterers in an isotropic host medium [26].

Most of the previous works discussed above are purely theoretical but, recent works have shown the relevance in several branches of physics of the experimental validation of the properties of analogous systems [27]. In this work using acoustic waves we show accurate experimental proofs of the properties of the periodic arrays made of rigid square-rod scatterers and propose applications for guiding and spatial filtering of acoustic waves. Specifically, we experimentally and theoretically analyse and make use of the tunability of the band gap in such a periodic structure made of rigid square-rod scatterers embedded in air. Due to the enlargement of the band gap for determined angles of rotation of the scatterers we can design tunable waveguides for frequencies within the band gap by changing the rotation angles of the scatterers in determined paths inside the array. The dispersion relations, i.e. the band structure of the periodic medium [5, 10], have been obtained using plane wave expansion (PWE) [28], whereas the scattering of waves in the finite periodic structures is analysed using finite element method (FEM) [29]. The approximation of supercell in the PWE is explicitly derived here for the case of square-rod scatterers and applied to analyse the case of waveguides. From the experimental point of view, a prototype made of 14 rows of seven rigid square-rod scatterers is used to validate the theoretical predictions. Some applications in waveguiding as well as a spatial-frequency filter based on the design of several waveguides with different guided frequencies are theoretically discussed in this work showing good agreement between experiments and proving the tunability of the system. In particular, the system could be used to improve the acoustic quality of music halls, and as a perspective as a superlens for audible sound.

The work is organized as follows. In section 2 we present the theoretical tools used in this work, i.e. PWE with supercell approximation and FEM. The experimental setup is presented in section 3 and the motivating results are shown in section 4. Section 5 shows both the theoretical and the experimental results of the spatial-frequency filters and waveguides analysed in this work. Finally, the conclusions are presented in section 6.

2. Theoretical tools

In this section we present the theoretical methods used to analyse a system composed of a 2D periodic arrangement of square-rod scatterers rotated by an angle θ as shown in figure 1(a). The scatterers are made of an isotropic solid A, embedded in an acoustic isotropic background B. The ratio between the area of the scatterer and the area of the unit cell is

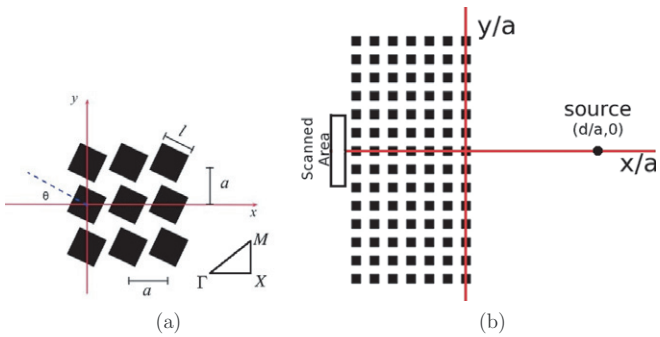

Figure 1. (a) Scheme of the system. The inset shows the first irreducible Brillouin zone of the 2D square periodicity. (b) Schematic view of the experimental set up. The scanned area depends on the experiment we analyse (see text for details).

called filling fraction, f. For the case analysed in this work, the lattice is made of rigid square-rod scatterers with side length l, embedded in a square periodicity with lattice constant a; so the filling fraction is $f = l^2/a^2$.

2.1. PWE: band structure

The medium considered in this work is invariant by translation in direction z, parallel to the symmetry axis of the scatterers, and exhibits a 2D periodicity in the transverse plane. By using this periodicity, it is possible to expand the physical properties of the medium in Fourier series and to use the Floquet–Bloch theorem to obtain the solution of the acoustic wave equation. Then, if these expansions in plane waves are substituted in the wave equation, one can obtain the following eigenvalue problem [28]

$$\sum_{\vec{G}'}((\vec{k}+\vec{G})\sigma_{\vec{k}}(\vec{G}-\vec{G}')(\vec{k}+\vec{G}')p_{\vec{k}}(\vec{G}') - \omega^2\eta_{\vec{k}}(\vec{G}-\vec{G}')p_{\vec{k}}(\vec{G}')) = 0, \quad (1)$$

where $\vec{k}$ is the wave vector, $\vec{G}$ is the 2D reciprocal-lattice vector, ω the angular frequency and $\sigma_{\vec{k}}$ ($\eta_{\vec{k}}$) are the amplitudes of the Fourier component $\vec{k}$ of $\sigma = \frac{1}{\rho} = \sum_{\vec{G}}\sigma_{\vec{k}}(\vec{G})e^{\imath\vec{G}\vec{r}}$ ($\eta = \frac{1}{\rho c^2} = \sum_{\vec{G}}\eta_{\vec{k}}(\vec{G})e^{\imath\vec{G}\vec{r}}$). It is usual to write that [28]

$$\beta_{\vec{k}}(\vec{G}) = \begin{cases} \beta^A f + \beta^B(1-f) & \text{if } \vec{G}=\vec{0}, \\ (\beta^A - \beta^B)\,F(\vec{G},\theta) & \text{if } \vec{G}\neq\vec{0}, \end{cases} \quad (2)$$

where $\beta = (\sigma, \eta)$, and $F(\vec{G},\theta)$ is the structure factor. For the case of square-rod scatterers of side l and angle of rotation θ embedded in a square unit cell, the structure factor is

$$F(\vec{G},\theta) = \frac{1}{A_{\text{uc}}}\int_{A_A} e^{-\imath\vec{G}\vec{r}}\,\overrightarrow{dr} = f\ \text{sinc}\left(\frac{\mathcal{G}_x l}{2}\right)\text{sinc}\left(\frac{\mathcal{G}_y l}{2}\right), \quad (3)$$

where,

$$\begin{pmatrix}\mathcal{G}_x\\ \mathcal{G}_y\end{pmatrix} = \begin{pmatrix}\cos(\theta) & \sin(\theta)\\ -\sin(\theta) & \cos(\theta)\end{pmatrix}\begin{pmatrix}G_x\\ G_y\end{pmatrix}, \quad (4)$$

and, A_{uc} is the area of the unit cell, A_{A} is the area of the considered scatterer and $\imath = \sqrt{-1}$. For $\vec{G}$ taking all the possible values, equation (1) constitutes a set of linear,

homogeneous equations for the eigenvectors $p_{\vec{k}(\vec{G})}$ and the eigenfrequencies $\omega(\vec{k})$.

Equation (1) can be expressed by the following matrix formulation

$$\sum_{i=1}^{3} \Gamma_i \Sigma \Gamma_i P = \omega^2 \Omega P, \tag{5}$$

where i=1,2,3. The matrices Γ_i, Σ and Ω are defined as

$$(\Gamma_i)_{mn} = \delta_{mn}(k_i + G_i^m), \tag{6}$$

or in the developed form,

$$\Gamma_i = \begin{pmatrix} k_i + G_i & 0 & \dots & 0 \\ 0 & k_i + G_i & \dots & 0 \\ \vdots & \vdots & \ddots & \vdots \\ 0 & \dots & \dots & k_i + G_i \end{pmatrix}, \tag{7}$$

$$\Sigma = \begin{pmatrix} \sigma(\vec{G}_1 - \vec{G}_1) & \dots & \sigma(\vec{G}_1 - \vec{G}_{N\times N}) \\ \vdots & \ddots & \vdots \\ \sigma(\vec{G}_{N\times N} - \vec{G}_1) & \dots & \sigma(\vec{G}_{N\times N} - \vec{G}_{N\times N}) \end{pmatrix}, \tag{8}$$

$$\Omega = \begin{pmatrix} \eta(\vec{G}_1 - \vec{G}_1) & \dots & \eta(\vec{G}_1 - \vec{G}_{N\times N}) \\ \vdots & \ddots & \vdots \\ \eta(\vec{G}_{N\times N} - \vec{G}_1) & \dots & \eta(\vec{G}_{N\times N} - \vec{G}_{N\times N}) \end{pmatrix}, \tag{9}$$

$$P = \begin{pmatrix} P(\vec{G}_1) \\ \vdots \\ P(\vec{G}_{N\times N}) \end{pmatrix}, \tag{10}$$

where $\vec{G} = (G_1, G_2, G_3) = (2\pi m/a, 2\pi n/a, 0)$. If $m = n = (-M, \dots, M)$, the size of the previous matrices is $N \times N = (2M+1) \times (2M+1)$.

By solving the system given in equation (5) for each Bloch vector in the irreducible area of the first Brillouin zone, $N \times N$ eigenvalues ω^2, are obtained and they can be used to represent the band structure $\omega(\vec{k})$.

2.1.1. Supercell approximation. In this approximation one considers an arrangement with primitive lattice vectors $\vec{a}_i$ ($i = 1, 2, 3$). Generally the supercell consists of a cluster of $n_1 \times n_2 \times n_3$ scatterers periodically placed in space. If we treat the supercell as the unit cell of the system, the primitive lattice vectors in the supercell approximation can be defined as $\vec{a'}_i = n_i \vec{a}_i$, and the complete set of lattices in the supercell approximation is $\{R' | R' = m_i \vec{a'}_i\}$, where n_i and m_i are integers. The primitive reciprocal vectors are then

$$\vec{b'}_i = 2\pi \frac{\varepsilon_{ijk} \vec{a'}_j \times \vec{a'}_k}{\vec{a'}_1 \cdot (\vec{a'}_2 \times \vec{a'}_3)}, \tag{11}$$

where ε_{ijk} is the three-dimensional Levi-Civita completely anti-symmetric symbol. The complete set of reciprocal lattice vectors in the supercell is $\{\vec{G} | \vec{G}_i = N_i \vec{b'}_i\}$ where N_i are integers. The reciprocal vectors represent the periodicity of the array in the reciprocal space. So, they depend on the periodicity of the unit cell, then for the case of the supercell one should define them taking into account all the scatterers in the supercell. Without loss of generality, the following formulation is constrained to 2D systems.

With the previous definition of the supercell, the equivalent expression to equation (2) for the case of the supercell approximation is shown here. The filling fraction of a square-rod scatterer in a supercell is $f^{\mathrm{S}} = l^2/A$, where A is the area occupied by the supercell. If we consider a supercell with N square-rod scatterers organized in an array of size $n_1 \times n_2$ then

$$\beta_{\vec{k}}(\vec{G}) = \begin{cases} \beta^A N\ f^{\mathrm{S}} + \beta^B (1 - N\ f^{\mathrm{S}}) & \text{if } \vec{G} = \vec{0}, \\ \left(\beta^A - \beta^B\right) F^{\mathrm{S}}(\vec{G}) & \text{if } \vec{G} \neq \vec{0}, \end{cases} \tag{12}$$

where $F^{\mathrm{S}}(\vec{G})$ is the structure factor of the supercell. It is worth noting that in equation (12) one takes into account the total number of scatterers in the supercell, N, in such a way that for $N = 1$, equation (12) reproduces equation (2).

In this approximation, the structure factor of the supercell has to be computed accounting for its size. If we consider a 2D array of scatterers with a supercell $n_1 \times n_2$, n_i being an odd number, the structure factor is expressed by

$$F^{\mathrm{S}}(\vec{G}, \theta) = \sum_{i=-\frac{(n_1-1)}{2}}^{\frac{(n_1-1)}{2}} \sum_{j=-\frac{(n_2-1)}{2}}^{\frac{(n_2-1)}{2}} \mathrm{e}^{\imath(ia|\vec{G}_1| + ja|\vec{G}_2|)} F(\vec{G}, \theta), \tag{13}$$

where $F(\vec{G})$ is given by equation (3) substituting f by f^{S}.

The interest of the supercell approximation in the PWE is the possibility to analyse point defects or waveguides in the structure [31, 32]. We consider now the case in which several point defects are created in periodic structures. Point defect can be understood as vacancies or square-rod scatterers with different side length, l, or with different rotating angle θ. Then, if the supercell presents N_p defects at the sites labelled by (n_s, m_s) in the periodic system, with $s = 1, \dots, N_p$, each one having a side length l_{s}, and a rotating angle θ_s, then the Fourier coefficients of the expansion of the physical parameters involved in the problem satisfy the following equation

$$\beta_{\vec{k}}(\vec{G}) = \begin{cases} \beta^A_{\vec{k}}((N - N_p) f^{\mathrm{S}} + f_{\mathrm{defect}}) + \\ +\beta^B_{\vec{k}}(1 - ((N - N_p) f^{\mathrm{S}} + f_{\mathrm{defect}})) & \text{if } \vec{G} = \vec{0}, \\ \left(\beta^A_{\vec{k}} - \beta^B_{\vec{k}}\right) F^{\mathrm{S}}(\vec{G}, \theta, \theta_{\mathrm{s}}) & \text{if } \vec{G} \neq \vec{0}, \end{cases} \tag{14}$$

where, $f_{\mathrm{defect}} = \sum_{s=1}^{N_p} l_s^2/A$. Notice that if we consider $l_s = 0$ $\forall s$, equation (14) becomes the case in which the defects are vacancies. The structure factor of such a supercell with N_p point defects is

$$\begin{aligned} F^{\mathrm{S}}(\vec{G}, \theta, \theta_s) = & \left(\sum_{i=-\frac{(n_1-1)}{2}}^{\frac{(n_1-1)}{2}} \sum_{j=-\frac{(n_2-1)}{2}}^{\frac{(n_2-1)}{2}} \mathrm{e}^{\imath(ia|\vec{G}_1| + ja|\vec{G}_2|)} \right) F(\vec{G}, \theta) \\ & - \left(\sum_{s=1}^{N_p} \mathrm{e}^{\imath(n_s a|\vec{G}_1| + m_s a|\vec{G}_2|)} \right) F(\vec{G}, \theta) \\ & + \sum_{s=1}^{N_p} \left(\left(\mathrm{e}^{\imath(n_s a|\vec{G}_1| + m_s a|\vec{G}_2|)} \right) F(\vec{G}, \theta_s) \right). \end{aligned} \tag{15}$$

Notice that the last term of equation (15) takes into account the presence of the defect, thus the structure factor (equation (3)) should be calculated using f_{defect}.

By introducing the previous expressions in the matrix formulation of the PWE, equation (5), the band structure of a periodic structure with and without defects using the supercell approximation can be calculated. The condition to apply the supercell approximation is that the defect interactions must be negligible between the neighbouring supercells. As a consequence, the size of the supercell should be large enough to place the defects sufficiently separated over consecutive supercells.

2.2. Finite elements method

The scattering of waves in finite structures in an unbounded domain is solved in this work using FEM. In these kinds of problems the Sommerfeld condition is analytically accomplished by the solutions of the problems. This basically assumes that no wave is reflected from infinity, and the solutions of these problems are called radiating solutions. Using FEM it is only possible to obtain some approximation of the radiating solutions in unbounded domains by applying some artificial boundaries in the numerical domain. Several techniques can be used for this purpose [29]. Among them the one of the perfectly matched layers (PMLs) [30] has been used here. PMLs have been applied to different cases based on the scalar Helmholtz equation [33], acoustics [34], elasticity [35], poroelastic media [36], water waves [37] and other hyperbolic problems [38], etc. Here, the interest is focused on the wave propagation in time-harmonic scattering problems for linear acoustics, i.e. on the scalar Helmholtz equation. It is worth noting here that the scatterers are considered rigid, so hard-wall (Neumann) boundary conditions have been assumed in the surfaces of the scatterers.

3. Experimental setup

The experimental results have been obtained in the anechoic chamber of LAUM (Laboratory of Acoustics at University of Maine). The experimental prototype consists of a 14×7 array of acoustically rigid square-rod scatterers made of wood, located on a square lattice with constant $a = 7.5\,\text{cm}$ (see figure 2(*b*)). The scatterers have a side length $l = 5\,\text{cm}$ ($l/a = 0.67$), therefore the filling fraction of the system is $f = l^2/a^2 = 0.44$. The scatterers are 2 m long, which is much bigger than the lattice constant and than the wavelength of interest in this work, so the system can be fulfilled when considered as 2D. The source has been placed at a distance $d = 1.5\,\text{m}$ ($d/a = 20$) away from the array in order to send a plane wave to the periodic array.

Figure 1(*b*) shows the schematic view of the experimental setup and figure 2 shows the pictures of three systems experimentally analysed in this work. Figures 2(*a*) and (*b*) correspond to the cases of complete periodic structures with the square-rod scatterers rotated by $\theta = 0^\circ$ and $\theta = 45^\circ$, respectively. Figure 2(*b*) shows the details of the fastening system of the array as well as the system of coordinates considered in this work. The picture of the array used to analyse the case of the waveguide can be observed in figure 2(*c*), in which one row of the array is rotated to 0° while the rest of the scatterers in the array are rotated to 45°.

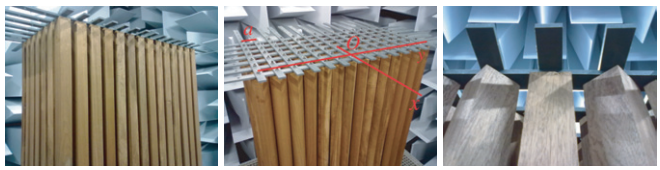

(a) (b) (c)

Figure 2. Experimental setup. Array made of rigid square-rod scatterers rotated by 0° (*a*) and 45° (*b*). Scatterers are 2 m long with a side length $l = 5\,5\,\text{cm}$. One can also see the details of the fastening system of the array. (*c*) Waveguide in the array made of square-rod scatterers rotated by 45°. The waveguide is generated by rotating one of the rows to 0°. The array has a square periodicity $a = 7.5\,\text{cm}$, and its size is 14×7 scatterers. The source is placed 1.5 m away from the array.

All the acoustic measurements are performed using a microphone B&K 1/4″ type 4135. The movement of the microphone in the anechoic chamber is controlled by a 1D robotized arm (Zaber LSQ) designed to move the microphone over a 1D trajectory in steps of 1 cm. The acquisition of the acoustic signal and the movement of the robotized arm are controlled by a Stanford SR 785 and Octave. Once the robotized system is turned off, the acoustic source generates a swept sine signal and the microphone detects it. The analyser provides the FFT information (module and phase for each frequency).

4. Motivating results: complete structures

In this section, we theoretically and experimentally analyse the dispersion relation, specially the band gaps, of a square array of rigid square-rod scatterers embedded in air ($\rho_{\text{air}} = 1.29\,\text{kg m}^{-3}$, $c_{\text{air}} = 340\,\text{m s}^{-1}$) depending on the angle of rotation of the scatterers. To avoid the overlapping between neighbour scatterers once they are rotated, the maximum length of the side of the square cross section should be $l = a/\sqrt{2}$. The filling fraction of the structure theoretically analysed in this section coincides with that of the prototype, i.e. $f = l^2/a^2 = 0.44$. We present the results using normalized units, i.e. normalized distances, $(x/a, y/a)$, and normalized frequencies, $\nu a/c_{\text{host}}$. Notice that the experimental results shown in this section constitute an accurate experimental study of the properties of 2D arrays made of square-rod scatterers due to the fact that the working frequencies of this work are less than 10% of the length of the scatterers, therefore the 2D approximation should be well fulfilled with a better accuracy than in previous works [39].

As has been theoretically shown in previous works [23], the band structure of square-rod scatterers is extremely dependent on the angle of rotation of the scatterers. One can go from the situation without full band gap to the case with large full band gap just by rotating the scatterers of the array. These peculiar band structures have been used in both photonics and acoustics in order to substantially improve the band gaps in 2D

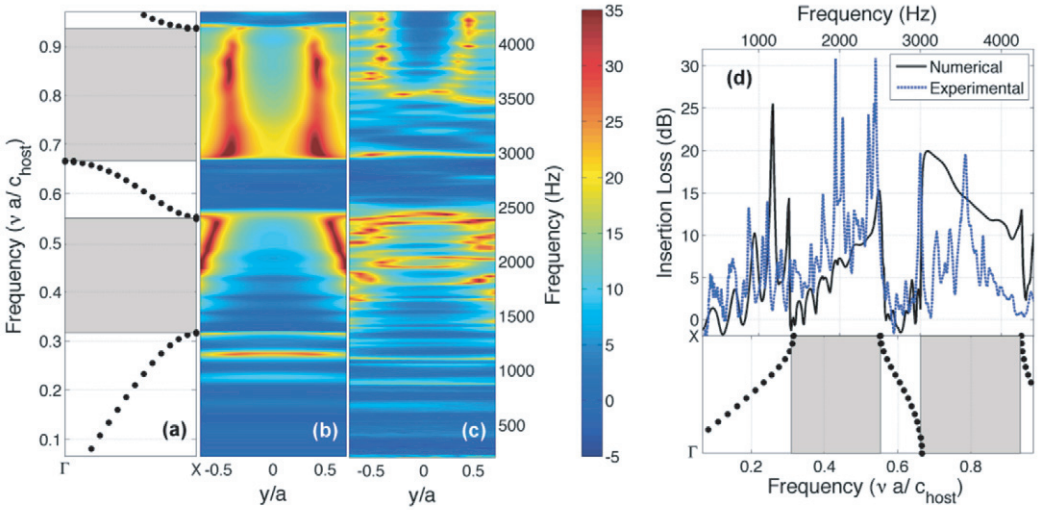

Figure 3. Numerical and experimental analysis of the propagation through a periodic array made of square-rod scatterers rotated 0° along the ΓX direction. (*a*) Band structure calculated using PWE. (*b*) Numerical and (*c*) experimental frequency-y map, evaluated at point $x/a = -8.67$ from the array. (*d*) Comparison of the spectra evaluated at $(x/a, y/a) = (-8.67, 0)$. Black continuous (blue dashed) line represents the numerical (experimental) IL spectrum. The lower panel shows the band structure for an easy comparison.

lattices. It has been shown that for square lattices, the largest absolute band gap using square-rod scatterers is wider than for the case of circular-rods [22]. Then, by means of simply rotating the square-rods, the scattering sections change and one can also manipulate the refraction properties of the system. Feng *et al* [40] observed that one can change from positive to negative refraction in these systems and thus produce a tunable acoustic superlens by rotating the scatterers [39]. These results show an effective method to control wave propagation in not only sonic crystals, but also other periodic structures, such as light in photonic crystals or water waves propagating through periodic rods.

At this stage we would like to show the accurate experimental validation of the tunability of the band gaps of this system. We analyse how the properties of the array can be drastically changed by rotating the square-rod scatterers and therefore without changing the lattice constant or the filling fraction. We study the particular cases of θ=0° and $\theta = 45°$. We then compare the band structure calculated using the PWE method with the numerical and experimental attenuation spectra of the finite structure. The attenuation spectrum is characterized in this work by means of the insertion loss (IL) defined as

$$\mathrm{IL} = 20\log_{10}\left(\frac{|p_{\mathrm{incident}}|}{|p_{\mathrm{incident}} + p_{\mathrm{scattered}}|}\right), \qquad (16)$$

where p_{incident} is the direct wave from the source and $p_{\mathrm{scattered}}$ is the scattered field by the array of square-rod scatterers, both fields evaluated in the same point. From the experimental point of view, we consider $|p_{\mathrm{incident}}|$ as the amplitude of the wave measured without the array and $|p_{\mathrm{incident}} + p_{\mathrm{scattered}}|$ the amplitude measured with the inserted array of square-rod scatterers.

Figures 3 and 4 show the comparison between the theoretical and experimental results for the cases of complete structures whose scatterers are rotated 0° and 45°, respectively. The band structures along the ΓX direction are shown in the (*a*) panels of figures 3 and 4. The scattering problem has been analysed in several points behind the structure. The IL spectrum has been calculated in the transversal sites $y/a = [-0.8, 0.8]$ at $x/a = -8.67$ (see figure 2(*b*) to see the coordinate system). The (*b*) panels of figures 3 and 4 show the IL frequency-y/a map obtained using FEM. In this map, each vertical line represents the IL spectrum for a given position $(x/a, y/a)$. Panels (*c*) of figures 3 and 4 show these experimental results. In the (*c*) panels the vertical axis shows the frequencies in Hz taking into account the lattice constant of the prototype and the sound velocity in the host (air). Then, one can compare normalized and real values in the same plot. Finally, panels (*d*) of figures 3 and 4 show the IL spectrum for the central point $(x/a, y/a) = (-8.67, 0)$. The black continuous line represents the numerical predictions and the blue dashed line represents the experimental results in the anechoic chamber. To have a clear comparison, we have also added the band structure in the bottom of the panels (*d*) of figures 3 and 4.

The case of $\theta = 0°$ does not present a full band gap (see [22, 23, 39]), however the band structure (see figure 3(*a*)) reveals two band gaps at ΓX direction between normalized frequencies 0.3157 (1431 Hz, experimentally) and 0.5529 (2506 Hz), and between 0.6653 (3016 Hz) and 0.9375 (4250 Hz). Between these two band gaps, a propagating band can be observed. The comparison between the band structure, figure 3(*a*), and the numerical frequency-y/a IL map, figure 3(*b*), shows agreement in the sense that in the range of frequencies where a band gap is predicted by the band structure, a range of attenuated frequencies appears in the case of the finite structure. It is worth noting that the attenuation is a function of the measurement point, but on average the band gaps appear in the range of frequencies predicted by the band

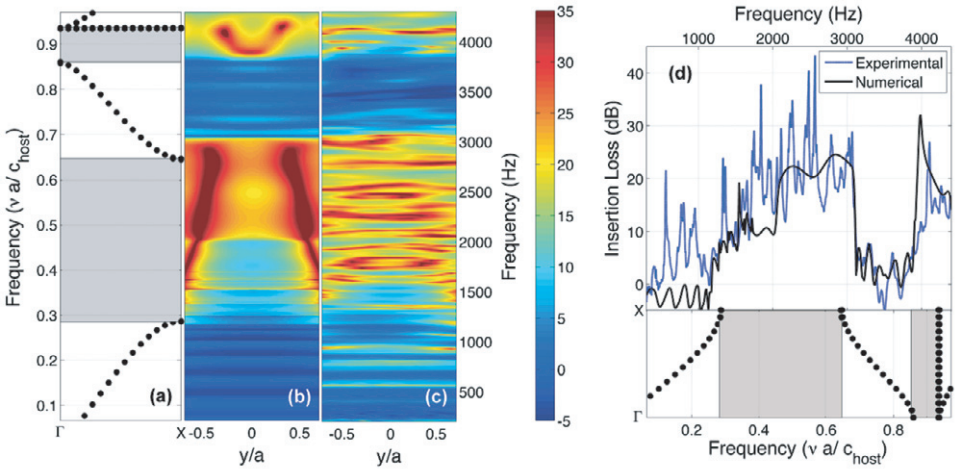

Figure 4. Numerical and experimental analysis of the propagation through a periodic array made of a square-rod rotated 45° along the ΓX direction. (*a*) Band structure calculated using PWE. (*b*) Numerical and (*c*) experimental frequency-y map, evaluated at point $x/a = -8.67$ from the crystal. (*d*) Comparison of the spectra evaluated at $(x/a, y/a) = (-8.67, 0)$. Black continuous (blue dashed) line represents the numerical (experimental) IL spectrum. The lower panel shows the band structure for an easy comparison.

structure. The propagating band is also well reproduced by the finite structure in agreement with the PWE predictions.

In figure 3(*c*) one can observe the frequency-y/a IL map measured in the anechoic chamber. Similar behaviour of the attenuation in the experimental results can be seen by comparing with the numerical predictions in figure 3(*b*). Due to the finite size of the structure one can also observe the presence of the well-known Fabry–Pérot resonances [10, 41], which are the effect of the multiple reflections inside the finite size crystal between the two interfaces. Figure 3(*d*) shows both the theoretical and experimental IL spectrum at central point $(x/a, y/a) = (-8.67, 0)$. Two band gaps and the transmission band are observed. Moreover, one can notice the presence of attenuated frequencies in the first propagating band. This is due to the refractive behaviour of the device at these ranges of frequencies, producing attenuation at the measurement point, but without presence of a bandgap.

For the case of $\theta = 45°$, figure 4, different properties than in the case of $\theta = 0°$ are predicted by the band structure (see [22, 23, 39]). For this structure a complete band gap is observed in the ΓX direction between frequencies 0.286 (1295 Hz) and 0.6463 (2930 Hz), and a second band gap at higher frequencies between 0.8575 (3887 Hz) and 0.936 (4243 Hz) is predicted. Notice that for this case the band gap at ΓX direction is wider than in the case of $\theta = 0°$. Between them, a propagating band wider than in the case of the $\theta = 0°$ is observed. Figure 4(*b*) shows the frequency-y/a IL map for the case of $\theta = 45°$ while figure 4(*c*) shows the measurements of the IL map in the anechoic chamber. Figure 4(*d*) shows both the theoretical and experimental IL spectrum for the central point $(x/a, y/a) = (-8.67, 0)$ in the case of $\theta = 45°$. The black line represents the numerical predictions and the blue dashed line shows the experimental results in very good agreement.

A good agreement between the properties theoretically predicted by the band structure and the attenuation properties numerically obtained using the finite structure is observed for the cases of $\theta = 0°$ and $\theta = 45°$ (figures 3 and 4, respectively). The differences between the numerical predictions and the experimental results could be the result of the errors in the positioning system, of the small curvature of the square-rod scatterers used in the prototype which are not perfectly straight (a relative error in the worst cases up to 12% at 0° and up to 70% at 45°) and also due to the fact that in the experimental situation a non perfectly plane wave impinges the crystal.

5. Results: waveguides

5.1. Simple waveguides

In this section the case of a waveguide in the 2D lattice of square-rod scatterers rotated by 45° is considered. The linear defect is generated by rotating the scatterers of a row with $\theta \neq 45°$ creating consequently a linear defect. Figure 5(*a*) shows a general scheme of the waveguide considered in this section. Figure 2(*c*) shows the experimental setup for the case in which the angle of the linear defect is $\theta_{\text{defect}} = 0°$.

Using the PWE with the supercell approximation, explicitly shown in section 2, the propagation properties of a 2D array made up of square-rod scatterers with a linear defect are analysed in this section. The supercell has a size of 1×5 scatterers with the linear defect in the middle. Figure 5(*a*) shows the supercell considered for the calculations. This supercell is long enough to avoid the interaction between the localized modes in neighbour linear defects. The complete structure is made of square-rod scatterers with $l = 0.67a$ and rotated $\theta = 45°$ in order to have a complete band gap. Therefore, conditions to enable guidance in linear defects at frequencies within the band gap are fulfilled.

From a general point of view, the linear defect could be created by introducing a row of square-rod scatterers with a different side length, l_{defect}, and a different angle of rotation, θ_{defect}. Figure 5(*b*) shows the general theoretical analysis of the dependence of the guided frequency on both the side length l_{defect}/a and the angle of rotation of the linear defect, θ_{defect}. We particularize here for the case in which the side length of the

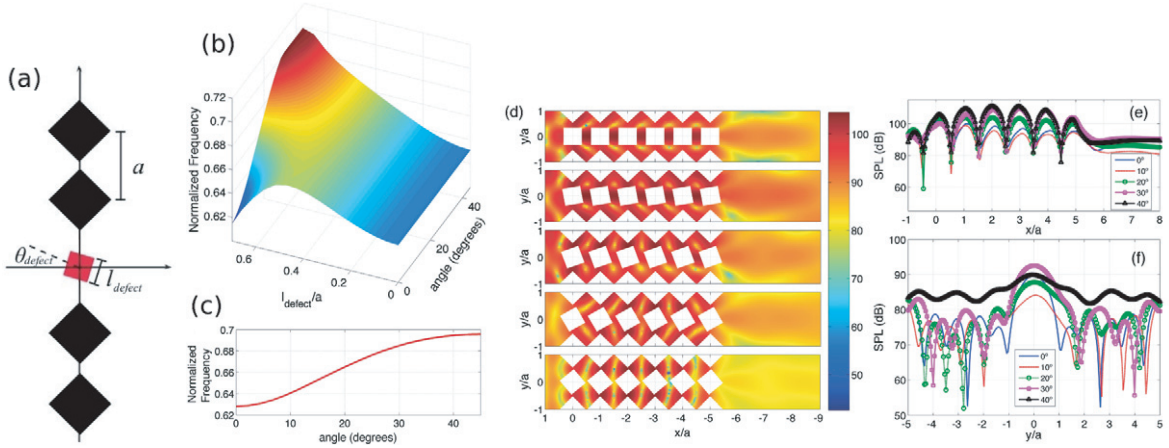

Figure 5. (*a*) Scheme of the supercell considered for the analysis of the waveguides. (*b*) General analysis of the frequency dependence of the guided mode on both the ratio l_{defect}/a and the rotating angle θ. (*c*) Dependence of the frequency of the guided mode for the case analysed in this work, $l_{\text{defect}}/a = l/a = \sqrt{f}$. (*d*)–(*f*) FEM simulation of the scattering problem by a finite structure made of 14×7 square-rod scatterers, in which the central row of cylinders has been rotated. (*d*) Sound pressure level (SPL) maps for several rotating angles of the central row. (0° (upper panel), 10°, 20°, 30°, 40° (lower panel)). (*e*) Longitudinal cut along the line x/a at $y/a = 0.5$, between the central row and the next one. (*f*) Transversal cut behind the crystal at $x/a = -8$ along the line y/a. Each coloured line represents the SPL for a determined rotating angle of the linear defect.

scatterers of the linear defect is $l_{\text{defect}}/a = l/a$, i.e. the same ratio as the square-rod scatterers of the complete structure. Then, only by rotating the row that constitutes the linear defect, can the guided frequency propagating through the waveguide be tuned. Figure 5(*c*) shows the dependence of the guided frequency for this case on the angle of rotation of the square-rod scatterer. Notice that all the frequencies represented in figure 5(*c*) belong to the band gap at each angle of rotation.

Figure 5(*d*) shows the sound pressure level (SPL) map for the cases where the scatterers of the linear defect are rotated 0°, 10°, 20°, 30° and 40° (from the top to the bottom of the panel, respectively). The guided frequencies correspond to the frequencies obtained by PWE with supercell approximation in figure 5(*c*). Between 0° and 30° there is propagation because the guided band is isolated inside the band gap. However, for larger angles, the propagating band is at the same frequency as the band gap edge, and the corresponding Bloch mode is excited inside the structure.

Figures 5(*e*) and (*f*) show the cuts along the x and y axis for each rotating angle of figure 5(*d*). Coloured lines represent the SPL profile in each direction. In figure 5(*f*) one can see a maximum value of SPL at point $y/a = 0$ for the waveguides whose angles are between 0° and 30°. At these angles the guided mode is confined in the waveguide. However, at 40°, although the SPL is higher, it is not confined at the waveguide because the mode is very close to the propagating mode in the second band.

For comparison between theoretical predictions and experimental results we particularize for the case where the scatterers in the linear defect are rotated 0°. If we consider that the linear defect is generated along the x axis and the origin of coordinates is as shown in figure 2(*b*), then we have measured and simulated the SPL spectrum at a point located in $x/a = -8$ and along the trajectory $y/a = [-2, 2]$.

Figure 6(*a*) shows the band structure for this particular case with the red dots showing the guided mode inside the bandgap at normalized frequency 0.627 (2841 Hz). In order to clearly see the wave guidance along this linear defect, we plot in figures 6(*b*) and (*c*) the experimental and numerical SPL maps, respectively. Each vertical line shows the SPL spectrum for a given y/a point. The maximum value of SPL at the frequency of guidance is observed at the point $y/a = 0$. The colour scale shows the SPL. It is worth noting that in the experimental map the values of frequency are not normalized, therefore, one can compare the real case with that theoretically predicted. Figure 6(*d*) shows both the experimental and numerical SPL profiles along the measured points in the y/a axis at the guidance frequency. The blue continuous line represents the numerical predictions, whereas the red dashed line shows the experimental values. Good agreement between the theoretical predictions and the experimental results is achieved.

5.2. *Spatial-frequency acoustic filter*

In the previous section we have shown the particular case of the linear defect with $\theta_{\text{defect}} = 0°$. It is worth noting that the analysis shown in figure 5(*c*) represents a powerful design tool, in such a way that one can design waveguides for a determined frequency just rotating the specific angle given by this design line. In this section we show an example of the tunability of such a system. In a square array made of square-rod scatterers with $\theta = 45°$, we generate three different waveguides by rotating three rows, each one with a different angle of rotation. We choose, for example, the angles $\theta_{1,\text{defect}} = 0°$, $\theta_{2,\text{defect}} = 18°$, $\theta_{3,\text{defect}} = 28°$ as shown in figure 7(*a*). Due to the fact that each angle is associated with different guided frequencies (see figure 5(*c*)), we expect different acoustic patterns behind the structure depending on the frequency.

Figure 7(*b*) shows the y/a-frequency SPL map. Each vertical line represents the field measured at $x/a = -8$ all along the points $y/a = [-7, 7]$ for a given frequency

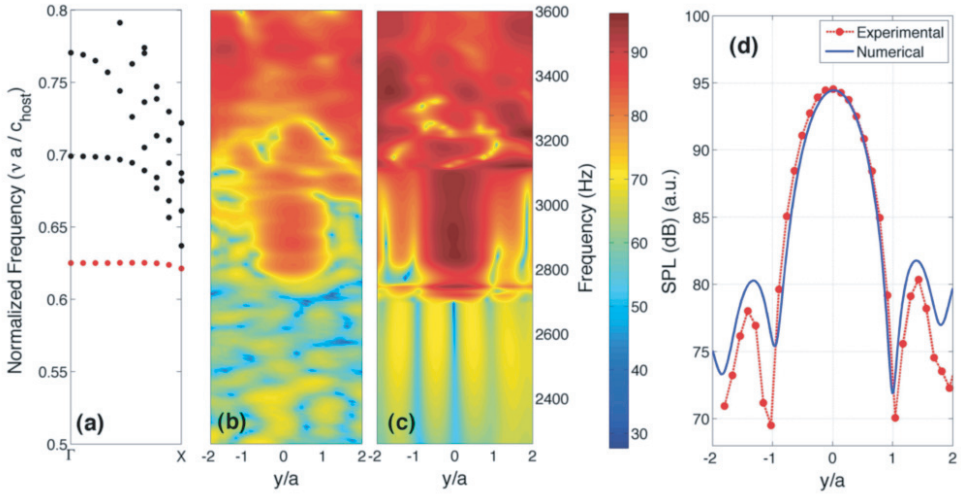

Figure 6. Numerical and experimental results of the waveguide made by rotating the scatterers of a row at 0°. (*a*) Band structure. Red dots represent the guided mode inside the band gap. (*b*) and (*c*) show the SPL measured and numerically simulated spectra for the several points along the y axis ($y/a = [-2, 2]$) at $x/a = -8$. (*d*) SPL profile at $x/a = -8$ at the guided frequency, 2841 Hz. Blue continuous line represents the numerical predictions and dashed red line shows the experimental results.

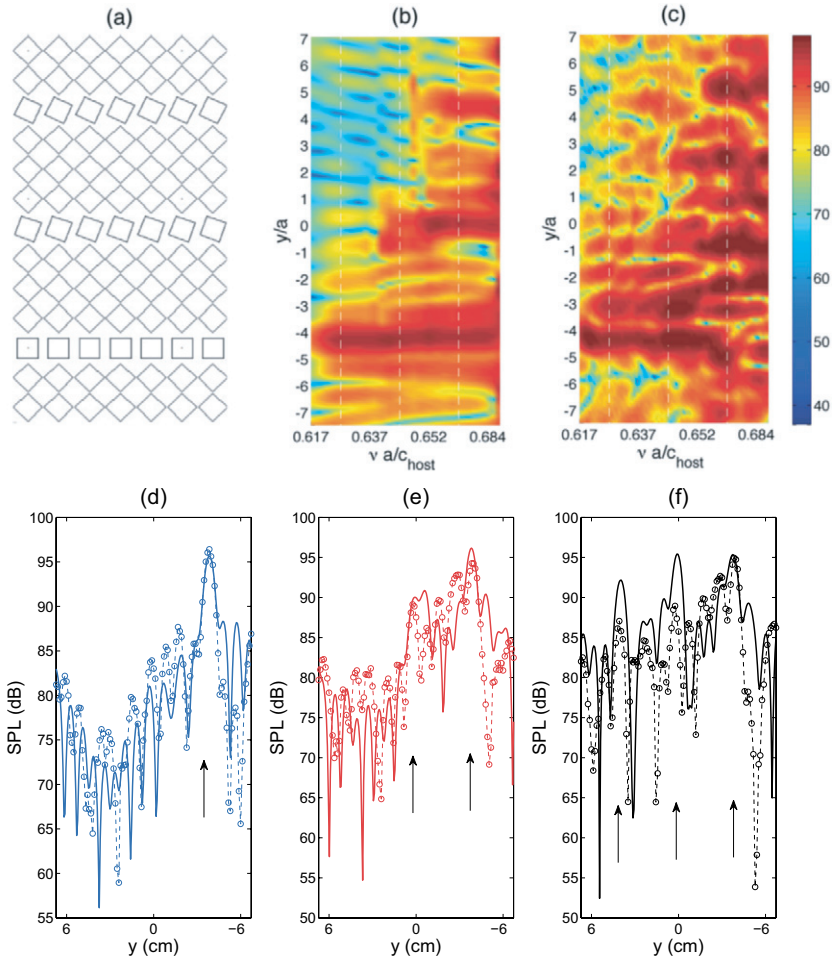

Figure 7. Spatial-frequency acoustic filter. (*a*) Scheme of the acoustic filter. (*b*) and (*c*) represent the numerical and the experimental results in dB of the y/a-frequency SPL maps, respectively. Colour scale represents the values of the SPL. Each vertical line represents the SPL values along the points $y/a = [-7,\ 7]$ at $x/a = -8$ for a given normalized frequency ($\nu a/c_{\text{host}}$). (*d*)–(*f*) represent the vertical cuts of the maps shown in (*b*) and (*c*) at the normalized frequencies 0.623, 0.648 and 0.675, respectively. Continuous lines are for the numerical predictions and dashed lines for the experimental results.

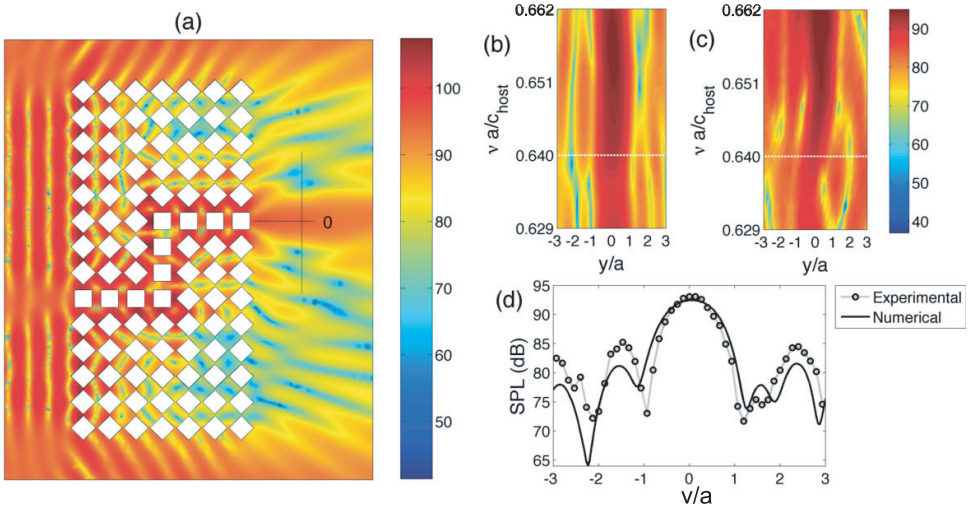

Figure 8. (*a*) Numerical SPL map at normalized frequency $va/c_{\text{host}} = 0.64$. The SPL in dB is shown in the colour scale. The black continuous line represents the measuring points. (*b*) and (*c*) show the numerical and experimental frequency-y/a SPL map, respectively. (*d*) Comparison of the numerically obtained SPL (black continuous line) with the experimental measurements (black dotted lines) measured in the point $x/a = -8$ at the frequency $va/c_{\text{host}} = 0.64$.

marked at the horizontal axis. The correspondence between the position of the waveguide and the position of SPL maximum values is striking. One can also see how the guided mode appears at these determined positions depending on the frequency. Figure 7(*c*) shows the experimental y/a-frequency SPL map. For a clear comparison between numerical and experimental results, we have plotted in figures 7(*d*)–(*f*) the vertical cuts of this y/a-frequency SPL map at the normalized frequencies 0.623, 0.648 and 0.675, respectively (marked also in figures 7(*b*) and (*c*) with dashed white lines). Continuous lines represent the numerical SPL and dashed lines represent the experimental results. One can see that for the low frequencies of the design line, only one transmitted peak behind the structure emerges in figure 7(*d*). At middle frequencies two transmitted peaks in figure 7(*e*) are observed. And, finally at high frequencies, three transmitted peaks exist (figure 7(*d*)). Arrows in figures 7(*d*) and (*e*) mark the positions where the sound is transmitted depending on frequency.

5.3. Guiding and splitting waves inside the SC

Due to the tunability of the system shown in this work, one can design several paths to guide the sound through the structure only by rotating the scatterers. In this section two different systems have been numerically and experimentally analysed. Figures 8(*a*) and 9(*a*) show the two cases analysed in this section. In the first one, sound is guided by a bended path and leaves the structure by one exit in a different y-position than the entrance. The second one consists of a bifurcated waveguide in which the sound is divided in two paths presenting two different exits, so showing the possibilities of splitting the waves in two different paths. The guided paths in both structures are generated by rotating the square-rod scatterers with $\theta_{\text{defect}} = 0^\circ$. The rest of square-rod scatterers in the array are fixed with $\theta = 45^\circ$.

Figure 8 shows the numerical and the experimental results for the case of the bended waveguide with one exit. Figure 8(*a*) shows the SPL map for one of the guided frequencies, $va/c_{\text{host}} = 0.64$. One can observe the guidance of the wave through the bended waveguide and the maximum value of SPL in the exit of the waveguide. Figure 8(*b*) and (*c*) represent the numerical and the experimental frequency-y/a SPL maps. It is easy to see the maximum values around $y/a = 0$, i.e. in front of the exit of the waveguide. For a better comparison between the numerical and experimental results, we plot the vertical cut along the points $y/a = [-3, 3]$ (following the coordinate axis shown in figure 8(*a*)) measured in the point $x/a = -8$ at the frequency $va/c_{\text{host}} = 0.64$ in figure 8(*d*). The black continuous line represents the numerical simulations whereas the black dashed line represents the experimental results. A fairly good agreement is observed.

Figure 9 shows the numerical and the experimental results for the case of the bifurcated waveguide with two exits. Figure 9(*a*) shows the SPL map for one of the guided frequencies, $va/c_{\text{host}} = 0.629$. The guidance of the wave through the bifurcated waveguide and the maximum value of SPL at the two exits of the waveguide are shown. Figures 9(*b*) and (*c*) represent the numerical and the experimental frequency-y/a SPL maps. The maximum values around $y/a = -3$ and $y/a = 3$, i.e. in the two ends of the bifurcated waveguide are clearly seen. For a better comparison between the numerical and the experimental results, we plot the vertical cut along the points $y/a = [-5, 5]$ (following the coordinate axis shown in figure 9(*a*)) measured in the point $x/a = -8$ at the frequency $va/c_{\text{host}} = 0.629$ in figure 9(*d*). Once again the observed good agreement demonstrates the possibility of waveguiding by defect complex waveguides.

6. Concluding remarks

In this work we use acoustic waves to experimentally proof the physical properties of modulated systems made of square-rod scatterers as well as to design applications for guiding and

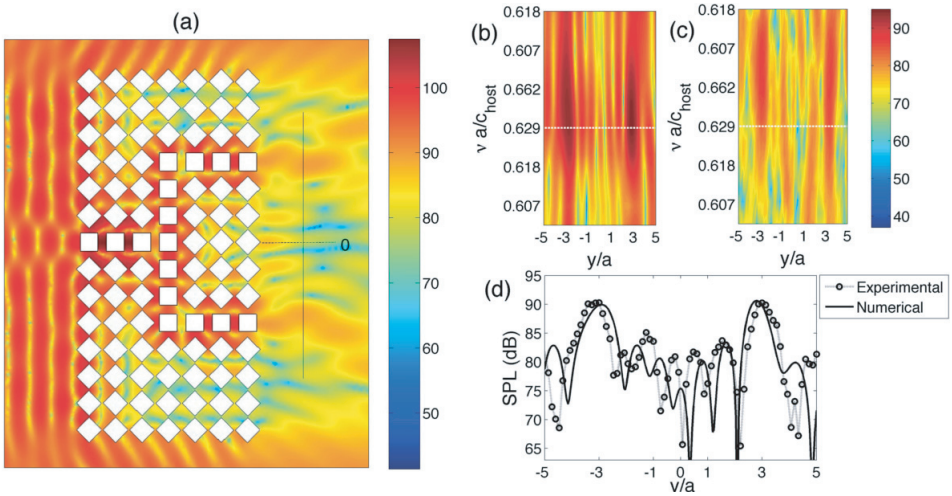

Figure 9. (*a*) Numerical SPL map at normalized frequency $va/c_{\text{host}} = 0.629$. The SPL in dB is shown in the colour scale. The black continuous line represents the measuring points. (*b*) and (*c*) show the numerical and experimental frequency-y/a SPL map, respectively. (*d*) Comparison of the numerical predictions of the SPL (black continuous line) with the experimental measurements (black dotted lines) measured in the point $x/a = -8$ at the frequency $va/c_{\text{host}} = 0.629$.

spatial filtering of acoustic waves. Extensive simulations and experimental results in order to show tunable waveguides made of arrays made of rigid square-rod scatterers embedded in air are performed here. We have experimentally and theoretically shown that by rotating some of the square-rod scatterers of an array one can easily produce a point defect, and even multiple point or line defects. This work could also be effectively extended to progressing toward the realization of tunable systems for light, liquid, and other waves, which will lead to great potential in ultrasonics, photoelectronics and so on. The tunability we demonstrated in this work could be applied to control not only the band gap and the waveguiding properties but also the refraction properties of the system. The use of such a device as superlens for audible sound could be a perspective.

Acknowledgments

This work was supported by MCI Secretaría de Estado de Investigación (Spanish government) and FEDER funds, under grant FIS 2011-29734-C02-01 and -02. VRG is grateful for the support of 'Programa de Contratos Post-Doctorales con Movilidad UPV del Campus de Eexcelencia Internacional (CEI-01-11)' and of the grant 'BEST2012' of the Generalitat Valenciana.

References

[1] Linton C M and Evans D V 1990 The interaction of waves with arrays of vertical circular cylinders *J. Fluid Mechanics* **215** 549–69
[2] Farhat M, Guenneau S and Enoch S 2009 Ultrabroadband elastic cloaking in thin plates *Phys. Rev. Lett.* **103** 024301
[3] Martínez-Sala R, Sancho J, Sánchez J V, Gómez V, Llinares J and Meseguer F 1995 Sound attenuation by sculpture *Nature* **378** 241
[4] Sánchez-Pérez J V, Caballero D, Martínez-Sala R, Rubio C, Sánchez-Dehesa J, Meseguer F, Llinares J and Gálvez F 1998 Sound attenuation by a two-dimensional array of rigid cylinders *Phys. Rev. Lett.* **80** 5325–8
[5] Sigalas M, Kushwaha M S, Economou E N, Kafesaki M, Psarobas I E and Steurer W 2005 Classical vibrational modes in phononic lattices: theory and experiment *Z. Kristallogr.* **220** 765–809
[6] Yablonovitch E 1987 Inhibited spontaneous emission in solid-state physics and electronics *Phys. Rev. Lett.* **58** 2059
[7] John S 1987 Strong localization of photons in certain disordered dielectric superlattices *Phys. Rev. Lett.* **58** 2486
[8] Kushwaha M, Halevi P, Dobrzynski L and Djafari-Rouhani B 1993 Acoustic band structure of periodic elastic composites *Phys. Rev. Lett.* **71** 2022–5
[9] Kushwaha M 1997 Stop-bands for periodic metallic rods: sculptures that can filter the noise *Appl. Phys. Lett.* **70** 3218
[10] Joannopoulos J, Johnson S, Winn J and Meade R 2008 *Photonic Crystals. Molding the Flow of Light* (Princeton, NJ: Princeton University Press) p 286
[11] Pennec Y, Vasseur J, Djafari-Rouhani B, Dobrzynski L and Deymier P A 2010 Two-dimensional phononic crystals: examples and applications *Surf. Sci. Rep.* **65** 229
[12] Sigalas M 1997 Elastic wave band gaps and defect states in two-dimensional composites *J. Acoust. Soc. Am.* **101** 1256
[13] Li X and Liu Z 2005 Coupling of cavity modes and guiding modes in two-dimensional phononic crystals *Solid State Commun.* **133** 397–402
[14] Laude V, Achaoui Y, Benchabane S and Khelif A 2009 Evanescent bloch waves and the complex band structure of phononic crystals *Phys. Rev.* B **80** 092301
[15] Romero-García V, Sánchez-Pérez J V, Castiñeira Ibáñez S and Garcia-Raffi L M 2010 Evidences of evanescent bloch waves in phononic crystals *Appl. Phys. Lett.* **96** 124102
[16] Sánchez-Morcillo V, Staliunas K, Espinosa V, Pérez-Arjona I, Redondo J and Soliveres E 2009 Propagation of sound beams behind sonic crystals *Phys. Rev.* B **80** 134303
[17] Khelif A, Choujaa A, Djafari-Rouhani B, Wilm M, Ballandras S and Laude V 2003 Trapping and guiding of acoustic waves by defect modes in a full-band-gap ultrasonic crystal *Phys. Rev.* B **68** 214301
[18] Sigalas M, Economou E and Kafesaki M 1994 Spectral gaps for electromagnetic and scalar weaves: possible explanation for certain differences *Phys. Rev.* B **50** 3393
[19] Caballero D, Sánchez-Dehesa J, Rubio C, Martínez-Sala R, Sánchez-Pérez J, Meseguer F and Llinares J 1999 Large two-dimensional sonic band gaps *Phys. Rev.* E **60** R6316

[20] Anderson C and Giapis K 1996 Larger two-dimensional photonic band gaps *Phys. Rev. Lett.* **77** 2949
[21] Anderson C and Giapis K 1997 Symmetry reduction in group 4 mm photonic crystals *Phys. Rev.* B **56** 7313
[22] Wang R, Wang X-H, Gu B-Y and Yang G-Z 2001 Effects of shapes and orientations of scatterers and lattice symmetries on the photonic band gap in two-dimensional photonic crystals, *J. Appl. Phys.* **90** 4307
[23] Goffaux C and Vigneron J P 2001 Theoretical study of a tunable phononic band gap system *Phys. Rev.* B **64** 075118
[24] Norris R C, Hamel J S and Nadeaua P 2008 Phononic band gap crystals with periodic fractal inclusions: theoretical study using numerical analysis *J. Appl. Phys.* **103** 104908
[25] Bilal O R and Hussein M I 2011 Ultrawide phononic band gap for combined in-plane and out-of-plane waves *Phys. Rev.* E **84** 065701(R)
[26] Lin S-C S and Huang T J 2011 Tunable phononic crystals with anisotropic inclusions *Phys. Rev.* B **83** 174303
[27] Lemoult F, Kaina N, Fink M and Lerosey G 2013 Wave propagation control at the deep subwavelength scale in metamaterials *Nature Phys.* **9** 55–60
[28] Kushwaha M, Halevi P, Martínez G, Dobrzynski L and Djafari-Rouhani B 1994 Theory of acoustic band structure of periodic elastic composites *Phys. Rev.* B **49** 2313–22
[29] Ihlenburg F 1998 *Finite Element Analysis of Acoustic Scattering* (New York: Springer) p 224
[30] Berenger J 1994 A perfectly matched layer for the absorption of electromagnetic waves *J. Comput. Phys.* **114** 185
[31] Sun J-H and Wu T-T 2006 Propagation of surface acoustic waves through sharply bent two-dimensional phononic crystal waveguides using a finite-difference time-domain method *Phys. Rev.* B **74** 174305
[32] Romero-García V, Sánchez-Pérez J V and Garcia-Raffi L M 2010 Propagating and evanesent properties of double-point defects in sonic crystals *New. J. Phys.* **12** 083024
[33] Harari I, Slavutin M and Turkel E 2000 Analytical and numerical studies of a finite element PML for the helmholtz equation *J. Comput. Acoust.* **8** 121–37
[34] Qi Q and Geers T 1998 Evaluation of the perfectly matched layer for computational acoustics *J. Comput. Phys.* **139** 166–83
[35] Basu U and Chopra A 2003 Perfectly matched layers for time-harmonic elastodynamics of unbounded domains: theory and finite-element implementation *Comput. Method Appl. Mech. Eng.* **33** 707–25
[36] Zeng Y, He J and Liu Q 2001 The application of the perfectly matched layer in numerical modeling of wave propagation in poroelastic media *Geophysics* **66** 1258–66
[37] Navon I, Neta B and Hussaini M 2004 A perfectly matched layer approach to the linearized shallow water equations models *Mon. Weather Rev.* **132** 1369–78
[38] Lions J L, Métral J and Vacus O 2002 Well-posed absorbing layer for hyperbolic problems *Numer. Math.* **92** 535–62
[39] Pichard H, Richoux O and Groby J-P 2012 Experimental demonstration in audible frequency range of band gap turability and negative refraction in two dimensional sonic crystals *J. Acoust. Soc. Am.* **132** 2816–22
[40] Feng L, Liu X P, Lu M H, Chen Y B, Chen Y F, Mao Y W, Zi J, Zhu Y Y, Zhu S N and Ming N B 2006 Refraction control of acoustic waves in a square-rod-constructed tunable sonic crystal *Phys. Rev.* B **73** 193101
[41] Sanchis L, Hakanson A, Cervera F and Sánchez–Dehesa J 2003 Acoustic interferometers based on two-dimensional arrays of rigid cylinders in air *Phys. Rev.* B **67** 035422